Biochemistry **2007,** *46,* 15062−15075

Dynamics of Backbone Conformational Heterogeneity in *Bacillus subtilis* Ribonuclease P Protein[†]

Christopher H. Henkels,[‡] Yu-Chu Chang, Stacy I. Chamberlin,[§] and Terrence G. Oas*

Department of Biochemistry, Box 3711, Duke University Medical Center, Durham, North Carolina 27710

Received July 20, 2007; Revised Manuscript Received October 15, 2007

ABSTRACT: Interconversion of protein conformations is imperative to function, as evidenced by conformational changes associated with enzyme catalytic cycles, ligand binding and post-translational modifications. In this study, we used ^{15}N NMR relaxation experiments to probe the fast (i.e., ps−ns) and slow (i.e., μs−ms) conformational dynamics of *Bacillus subtilis* ribonuclease P protein (P protein) in its folded state, bound to two sulfate anions. Using the Lipari−Szabo mapping method [Andrec, M., Montelione, G. T., and Levy, R. M. (2000) *J. Biomol. NMR 18*, 83−100] to interpret the data, we find evidence for P protein dynamics on the μs−ms time scale in the ensemble. The residues that exhibit these slow internal motions are found in regions that have been previously identified as part of the P protein−P RNA interface. These results suggest that structural flexibility within the P protein ensemble may be important for proper RNase P holoenzyme assembly and/or catalysis.

Ribonucleoprotein (RNP) complexes are involved in a wide variety of critical cellular processes including translation, mRNA splicing, telomere maintenance, membrane targeting, and tRNA maturation. However, the thermodynamic and kinetic principles that drive and stabilize the formation of RNP architectures are poorly understood. Generally, RNA tertiary structure is relatively unstable (*1*) so one major role of the protein is to facilitate proper RNA folding and/or stabilize active ribozyme conformations. This is the case for the group I self-splicing intron bI5 from yeast mitochondria, which requires the presence of the protein cofactor CBP2 to stabilize the active ribozyme conformation under physiological conditions (*2*, *3*). Alternatively, RNA can provide the stable structural scaffold onto which an unstable protein can fold. Examples of this phenomenon include the N protein from bacteriophage λ and the M domain of *Escherichia coli* Ffh. N protein is unstructured in the absence of its binding partner, however it forms a local α-helical structure upon binding box B RNA (*4*, *5*). The M domain is a molten globule sensitive to proteolysis; however, binding of 4.5S RNA causes the M domain to fold into a unique folded structure that is resistant to protease treatment (*6*). Thus, the strategies to stabilize specific RNP complexes are diverse. However, one common feature in almost every RNA−protein interaction studied to date is the presence of a conformational change in the protein subunit, in the RNA subunit, or in both macromolecules (for review, see (*1*, *7*, *8*)). Thus, RNP assembly is best described as an “induced fit”, a “conformational capture”, or a “ligand-induced conformational change” process. All of these terms describe local intramolecular changes thermodynamically coupled to intermolecular interaction (*7*).

From a statistical mechanical point of view, a protein conformational state consists of an ensemble of structures. The population of each member of this ensemble is determined by its individual free energy. (*9*). Thus even in the absence of ligand, conformations with high affinity for a ligand may already exist within the protein ensemble, even if they have high energy and are therefore poorly populated. Ligands, such as RNA, can specifically bind the poorly populated, ligand-complementary conformation. Binding to this conformation removes it from the unbound ensemble causing repopulation of binding-competent conformations from binding-incompetent ones.

If the energy difference separating various protein conformational states is sufficiently low, poorly populated conformations may be observed under solution NMR conditions (*10*, *11*). An example of this phenomenon is the N-terminal RNA recognition domain (RRM) of human U1A binding to the 3′-UTR of U1A mRNA. In the absence of RNA, backbone and side-chain relaxation experiments reveal conformational heterogeneity on the μs−ms time scale in the regions that bind RNA (loop 3); U1A has multiple conformations within the native state ensemble. These motions are quenched upon RNA binding which suggests that U1A maintains a rigid structure upon complex formation (*12*). Interestingly, the corresponding nucleotides on RNA become rigidified upon U1A−RNA interaction (*13*) so that conformational fluctuations of both U1A and its target RNA are suppressed in favor of a unique, rigid RNP interaction surface. Solution NMR spectroscopy is a good technique to detect protein motions on both the fast internal ps−ns time scale (e.g., bond vibrations) and on the slow internal μs−

[†] Supported by National Institutes of Health Grant GM45322.

* To whom correspondence should be addressed. Tel: (919) 684-4363. Fax: (919) 684-8885. E-mail: oas@duke.edu.

[‡] Present address: Department of Biochemistry and Molecular Genetics, Box 800733, University of Virginia Health Sciences Center, Charlottesville, VA 22908.

[§] Present address: Department of Chemistry, Campus Box 3290, Caudill and Kenan Laboratories, The University of North Carolina at Chapel Hill, Chapel Hill, NC 27599.

10.1021/bi701425n CCC: $37.00

ms time scale (e.g., local/global conformational changes) (for review, see (*10*, *14*−*16*)).

Here, we use NMR spectroscopy to probe the internal motional properties of *Bacillus subtilis* ribonuclease P (RNase P) protein (P protein) over a wide range of time scales. P protein is the noncatalytic, highly basic protein that associates with its cognate P RNA ribozyme to form the RNase P holoenzyme. RNase P is the endoribonuclease responsible for the 5′ maturation of precursor-tRNA (pre-tRNA) transcripts (for review, see (*17*, *18*)). Although P protein does not contain the catalytic components of RNase P, it is essential for *in vivo* catalysis (*19*). P protein has also been shown to stabilize P RNA structure (*20*−*22*), modulate substrate specificity (*23*), and enhance the affinity of magnesium ions required for catalysis (*24*). P protein also enhances RNase P holoenzyme catalytic efficiency through the direct interaction of the protein with the 5′-leader sequence of pre-tRNA (*25*−*27*).

Like many of the systems described above, P protein is unstable in the absence of ligand, but folds to a stable native state when bound to RNA or small multivalent anions. ^{15}N relaxation experiments were carried out to probe the local backbone fluctuations of P protein refolded in 20 mM sulfate. Using the Lipari−Szabo mapping method (*28*) to interpret the data, we find the presence of conformational heterogeneity (i.e., motions) on the μs−ms time scale in the native state ensemble. These residues map onto a specific region of P protein's surface. This surface correlates with the putative P protein−P RNA interface suggesting that the motions within the native ensemble may be important for proper RNase P holoenzyme assembly and/or catalysis.

EXPERIMENTAL PROCEDURES

Sample Preparation. The overexpression, purification, qualitative purity analyses, and quantitation of ^{15}N-labeled P protein (^{15}N-P protein) has been described elsewhere (*29*). The sample used for ^{15}N backbone relaxation experiments contained ~1 mM ^{15}N-P protein, 20 mM sodium sulfate, 0.02% (wt/vol) sodium azide, 10 mM sodium cacodylate (pH 6), and 20 μg/mL TMSP in 90% H_2O/10% D_2O.

NMR Spectroscopy. All ^{15}N relaxation experiments were performed at 25 °C on a Varian INOVA 600 MHz spectrometer equipped with a shielded *z*-field gradient coil. The gradient-enhanced, sensitivity-enhanced ^{15}N relaxation pulse sequences developed by Kay and co-workers (*30*) were used. Longitudinal relaxation times, T_1, were determined using the eight inversion recovery delay times in the following order: 274, 33, 1214, 503, 66, 810, 131, and 1991 ms. Transverse relaxation times, T_2, were determined using the following seven CPMG delay times in the exact order: 186, 16, 93, 248, 62, 124, and 30 ms. Both the T_1 and T_2 series of relaxation experiments were performed twice. Steady-state ^{15}N{^{1}H}-NOE values were determined from spectra that were recorded with (NOE) and without (noNOE) a 3 s ^{1}H-presaturation delay period within the recycle delay. NOE and noNOE spectra were collected in triplicate. All of the spectra were recorded with 2048 × 256 complex points; 16 transients were used per increment in the T_1 and T_2 experiments while eight scans were used per increment for the noNOE and the NOE spectra. Spectral windows of 10000 and 1500 Hz were used for the ^{1}H-dimension and the ^{15}N-dimension respectively.

Data Processing. All spectra were processed using nmrPipe (*31*). The ^{1}H dimension was zero-filled to 4096 points while the indirectly detected ^{15}N dimension was zero-filled to 512 points. Both dimensions were apodized with shifted sine-bell functions, Fourier-transformed, and the amide proton region was extracted for a final 2048 (^{1}H) × 512 (^{15}N) matrix. The processed spectra were analyzed with nmrDraw (*31*) to verify cross peak phases. Finally, cross peak intensities were measured and tabulated by nmrView (*32*).

The T_1 and T_2 times were obtained by fitting the cross peak intensity over the time delay series, $I(t)$, to a two-parameter single-exponential decay function $I(t) = I(0)\exp(-t/T_{1,2})$ where $I(0)$ is the best-fit value for the peak intensity at zero time. Nonlinear least-squares fit analysis was achieved using Kaleidagraph (Synergy Software, Reading, PA), and the standard errors for the relaxation times were determined from the uncertainty of the fits. The average T_1 and T_2 times were calculated from the best fits to the replicate time series and the standard error was propagated accordingly. The steady-state NOE was determined from the peak intensity ratio of the NOE spectrum over the noNOE spectrum. The final ^{15}N{^{1}H}-NOE and the corresponding uncertainty was determined from the average of the triplicate ratios.

Analysis of Relaxation Data via Reduced Spectral Density Mapping. The dependences of ^{15}N-R_1, ^{15}N-R_2, and ^{15}N{^{1}H}-NOE on the spectral density function for the amide ^{15}N−^{1}H spin pair are (*33*, *34*)

$$R_1\ (=T_1^{-1}) = (d^2/4)[J(\omega_H - \omega_N) + 3J(\omega_N) + 6J(\omega_H + \omega_N)] + c^2J(\omega_N) \quad (1)$$

$$R_2\ (=T_2^{-1}) = (d^2/8)[4J(0) + J(\omega_H - \omega_N) + 3J(\omega_N) + 6J(\omega_H) + 6J(\omega_H + \omega_N)] + (c^2/6)[3J(\omega_N) + 4J(0)] \quad (2)$$

$$\mathrm{NOE} = 1 + (d^2/4)(\gamma_H/\gamma_N)[6J(\omega_H + \omega_N) - J(\omega_H - \omega_N)]T_1 \quad (3)$$

$$d = [\mu_o h\gamma_N\gamma_H/(8\pi^2)]\langle 1/r_{NH}{}^3\rangle \quad (4)$$

$$c = \Delta(\omega_N/(3^{1/2})) \quad (5)$$

The parameters *d* and *c* reflect the magnitude of the amide NH bond dipolar coupling interaction and the chemical shift anisotropy respectively. In eq 4, μ_o is the permeability of free space, $\gamma_{H,N}$ are the gyromagnetic ratios for the ^{1}H and the ^{15}N nuclei, *h* is Plank's constant, and r_{NH} is the length of the amide bond. In eq 5, Δ is the ^{15}N chemical shift anisotropy. The amide bond vector distance r_{NH} was taken to be 1.02 Å, and the ^{15}N chemical shift anisotropy term Δ was taken to be 160 ppm (*35*). Therefore, the *d* and *c* values were calculated to be -7.21×10^4 Hz and -3.53×10^4 Hz, respectively, for experiments carried out on a 600 MHz (14.1 T) spectrometer. $J(\omega)$, the spectral density function, is a spectral analyzer that expresses the probability distribution of motional frequencies experienced by (amide NH) bond vectors undergoing stochastic processes. Therefore, the three experimentally measured relaxation parameters can be considered as "sampling", or "mapping onto", the spectral density function at the five specific frequencies (*34*, *36*).

It is clear from eqs 1−3 that the determination of three relaxation parameters at one spectrometer frequency does

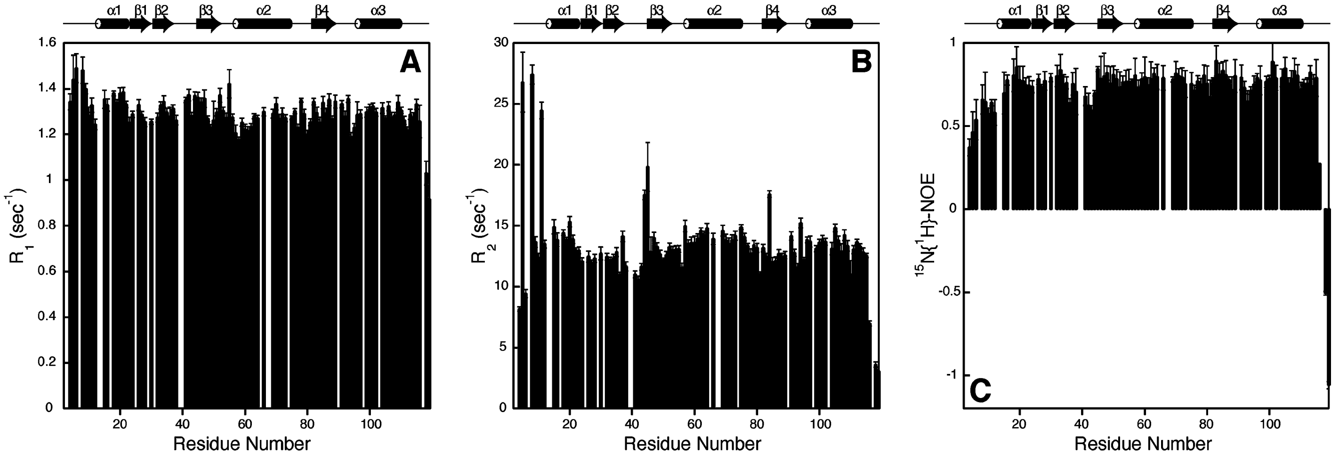

FIGURE 1: Backbone dynamics of P protein refolded in 20 mM sulfate based on ^{15}N relaxation data. ^{15}N longitudinal (A) and transverse (B) relaxation rates and ^{15}N{^{1}H}-NOE values (C) are plotted as a function of residue number. The relaxation data was recorded on a 14.1 T (600 MHz) spectrometer. Secondary structural elements identified in the crystal structure of P protein (*53*) are shown schematically.

not allow for the precise solution of the five spectral densities. However, previous studies have demonstrated that the contributions of the high-frequency terms, $J(\omega_H)$, $J(\omega_H + \omega_N)$, and $J(\omega_H - \omega_N)$, to the relaxation rates are roughly equivalent (*37*, *38*). Therefore, all of the high-frequency spectral densities (i.e., $J(\omega_H)$ and $J(\omega_H \pm \omega_N)$) can be substituted by a single spectral density term $J(\omega_H)$. This "reduced spectral density mapping" method (*36*, *39*) then permits the facile analytical calculation of $J(0)$, $J(\omega_N)$, and $J(\omega_H)$ from a single set of T_1, T_2, and ^{15}N{^{1}H}-NOE values. Furthermore, the single high-frequency spectral density term is given as $J(0.87\omega_H)$ under the approximation that $J(\omega) \sim 1/\omega^2$ (Method 1 in (*36*)). The resulting expressions for $J(0)$, $J(\omega_N)$, and $J(0.87\omega_H)$ are then derived through the inversion of eqs 1−3.

$$J(0.87\omega_H) = R_1(\mathrm{NOE} - 1)(\gamma_N/\gamma_H)(4/5)d^2 \qquad (6)$$

$$J(\omega_N) = \{R_1 - J(0.87\omega_H)(7d^2 - 4)\}/\{(3d^2/4) + c^2\} \qquad (7)$$

$$J(0) = \{R_2 - J(\omega_N)(3d^2/8 + c^2/2) - J(0.87\omega_H)(13d^2/8)\}/\{d^2/2 + 2c^2/3\} \qquad (8)$$

The errors from the relaxation parameters were propagated (*40*) to calculate the uncertainty of the spectral densities.

RESULTS

The ^{1}H and ^{15}N chemical shift frequencies have been determined for all 111 backbone amide NH groups that give rise to cross peaks in the HSQC spectrum of P protein. Although there are 118 residues in the *B. subtilis* version of P protein, three residues are not expected to give rise to cross peaks (P39, P90, and the NH$_2$-terminal A2) and four more residues are not present in any type of backbone assignment experiment (H3, R7, N13, and E14). Several pairs of residues have overlapping cross peaks (Q17/E40, S25/I67, R29/F31, R65/L103, R68/S117, and E74/E98) and were removed from subsequent analysis. The ^{15}N relaxation rates and ^{15}N{^{1}H}-NOEs for the remaining 99 well-resolved resonances are reported.

Backbone ^{15}N Relaxation. Four of the missing resonances correspond to residues found within the first thirteen residues of P protein. An extensive screen of solution conditions (pH, protein or ligand or salt concentration, and temperature) did not result in the observation of any of the missing resonances (Table S1, Supporting Information). One possible explanation for missing resonances is chemical exchange between two (or more) conformations on the microsecond to millisecond time scale. To characterize these and other time scale dynamics, the standard set of ^{15}N relaxation experiments (T_1, T_2, and ^{15}N{^{1}H}-NOE) were carried out on sulfate-refolded P protein.

The observed change in amide cross peak intensity is well described by the two-parameter single-exponential decay equation for the ^{15}N-T_1 and ^{15}N-T_2 experiments. Best-fit values for T_1 and T_2 were averaged over two replicates; the standard error for the average relaxation times was determined to be ~2% and ~3% respectively. The steady-state ^{15}N{^{1}H}-NOE was derived from the peak intensity ratio of amide NH cross peaks in the presence of a ^{1}H presaturation pulse to those without the pulse. The experiment was run in triplicate, and the average ^{15}N{^{1}H}-NOE is reported; the standard error for the average ^{15}N{^{1}H}-NOE values was ~9%. The observed ^{15}N relaxation parameters for the 99 well-resolved residues are shown in Figures 1A−C (see Table S2, Supporting Information for the corresponding data). The average values for R_1, R_2 and ^{15}N{^{1}H}-NOE are 1.29 ± 0.07 s^{-1}, 13.36 ± 3.13 s^{-1}, and 0.72 ± 0.24 respectively. There is not much deviation from the average R_1 value among residues except at the N- and C-terminus, where R_1 is higher and lower, respectively. Relatively constant R_1 values are commonly observed, and it is generally difficult to interpret the motions that give rise to the subtle deviations from the R_1 average. In contrast, excursions from the average R_2 and NOE values lend a more direct interpretation of internal amide NH bond motions. For example, the lower-than-average NOE values found at the termini of P protein are likely to be caused by increased motions on the ps−ns time scale; low and sometimes negative ^{15}N{^{1}H}-NOEs are observed for disordered regions. Elevated R_2 values, which are indicative of conformational processes on the μs−ms time scale, are observed for two residues (L44 and R45) at the intersection of the metal-binding loop and β-strand 3 intersection and one position within β-strand 4 (I84). High R_2 values are also observed for three residues within the first 13 residues (K5, N8 and K11), which, in

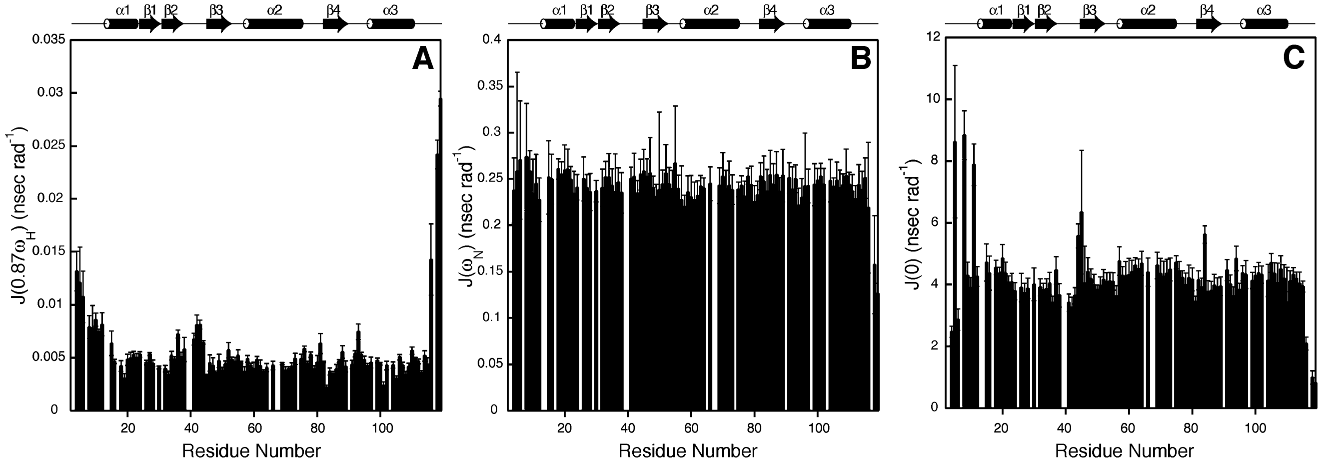

FIGURE 2: Reduced spectral density mapping analysis of P protein using the ^{15}N relaxation data in Figure 1 and eqs 6−8. The spectral density function is sampled at three frequencies, 0, 60.8, and 521.8 MHz; the latter two values correspond to ω_N and $0.87\omega_H$ on the 600 MHz spectrometer used to collect the data. The spectral densities $J(0.87\omega_H)$, $J(\omega_N)$, and $J(0)$ are displayed as a function of protein sequence in (A), (B), and (C) respectively. Note that the magnitudes of the spectral densities vary by several orders of magnitude. The secondary structure of P protein is shown as in Figure 1.

combination with the four missing amide peaks, provides strong evidence for conformational heterogeneity at the N-terminus of P protein on the μs−ms time scale.

Reduced Spectral Density Mapping. The observed relaxation rates are dependent on motions whose frequencies vary over several orders of magnitude (eqs 1−3). Therefore, the reduced spectral density mapping approach (see Experimental Procedures) was applied to extract the relative contributions of motions at $\omega = 0$, ω_N, and $0.87\omega_H$ to ^{15}N relaxation rates. The $J(0.87\omega_H)$, $J(\omega_N)$, and $J(0)$ spectral density values observed for each resonance are shown in Figures 2A−C (see Table S3, Supporting Information for the corresponding data). Generally, there is little deviation in the spectral densities of individual residues from the average values over the length of the protein. The average $J(0)$, $J(\omega_N)$, and $J(0.87\omega_H)$ values are 4.21 ± 1.03, 0.242 ± 0.018, and 0.0056 ± 0.0036 ns/radian, respectively; while the standard deviation for the calculated spectral densities are 10%, 10%, and 9%, respectively. Local regions that have internal motions on the ps−ns (i.e., fast) time scale typically display higher than average $J(0.87\omega_H)$ values and lower than average $J(0)$ values (*41*, *42*). This behavior is observed for residues at both termini of P protein and is characteristic of disordered protein regions. Slower motions, such as those caused by chemical exchange on the μs−ms (i.e., slow) time scale, are observed for residues that have larger than average $J(0)$ values while maintaining representative high-frequency spectral densities values ($J(0.87\omega_H)$ and $J(\omega_N)$). This behavior is observed at the same sites that have elevated R_2 relaxation rates, specifically N-terminal residues K5, N8, K11, β2-β3 loop/β-strand 3 intersection residues L44 and R45, and β-strand 4 residue I84. These results are consistent with the observation that these residues have the broadest resonances in the HSQC spectrum (data not shown).

Interpretation of $J(\omega_N)$ and $J(\omega_{0.87H})$ via Lipari−Szabo Mapping. Although the reduced spectral density method is computationally straightforward, this method provides no way to separate the relative contributions of internal amide NH bond motions from overall global tumbling to the observed $J(\omega)$ values. The popular "model-free" formalism derived by Lipari and Szabo (*43*, *44*), on the other hand, does permit the deconvolution of the relative effect of these motions on ^{15}N relaxation. This approach assumes a simple mathematical relationship between the spectral density function and the rates and relative magnitudes of overall protein tumbling and the internal amide NH bond motions. The "simple model-free" (SMF) equation gives $J(\omega)$ as the sum of two Lorentzian functions:

$$J(\omega) = (2/5)[\{S^2\tau_m/(1 + (\omega\tau_m)^2)\} + \{(1 - S^2)\,\tau/(1 + (\omega\tau)^2)\}] \quad (9)$$

where τ_m is the global tumbling correlation time; S^2 is the generalized order parameter that describes the degree of spatial restriction of the N−H bond vector whose internal motions are described by the effective correlation time τ_e which is related to τ through the relationship $1/\tau = 1/\tau_m + 1/\tau_e$. By this model, an N−H with an S^2 of 1 has no internal motion whereas an N−H with an order parameter of 0 would exhibit isotropic motion on the fast (ps−ns) time scale. Typically, a rigorous statistical analysis is required to determine the model-free parameters (τ_m, τ_e, and S^2) that minimize the difference between the predicted and observed relaxation parameters (T_1, T_2, and ^{15}N{^{1}H}-NOE) for each backbone ^{15}N (*45*).

Further extensions to eq 9 have been proposed. The "extended model-free" (EMF) formalism derived by Clore and co-workers includes a second-order parameter (S_f^2) that accounts for the possibility of two distinct time scales of internal bond motion faster than global tumbling (*46*). Chemical exchange contributions (R_{ex}) can also be included as an additional contribution to R_2. A potential problem with the model-free fitting strategy is that there can be up to four parameters to be fit to three observables. Typically, τ_m is fixed to permit more complex models than eq 9 to be used, if necessary. However, the fixed τ_m is based on an analysis of the relaxation data and not determined from an alternate, independent technique. Thus, there is the potential for cross correlation between the best fit model-free parameters and the fixed correlation time (see Figure 8 in (*28*)). A related problem with the model-free analysis is that, although the decision is statistical in nature, the inclusion of either R_{ex} or

S_f^2 can adversely affect the S^2 calculation (*47*) or predict motions that do not exist (*48*).

Therefore, a method that can depict the physically interpretable Lipari−Szabo model-free parameters from the analytically determined reduced spectral densities without resorting to least-squares fitting makes data interpretation more reliable. The "Lipari−Szabo mapping" method devised by Andrec et al. (*28*) is such a technique. It employs simple graphical relationships to analytically derive S^2 and τ_e from the high-frequency spectral densities ($J(\omega_N)$ and $J(0.87\omega_H)$). Thus, the potential artifacts that chemical exchange (R_{ex}) may have on S^2 are eliminated. This is particularly important for sulfate-folded P protein because the data suggest the presence of conformational heterogeneity on the μs−ms time scale in the biologically relevant N-terminal region of the protein (see Discussion).

One prerequisite for Lipari−Szabo mapping is an estimate of the global correlation time τ_m. The method of Kay and co-workers (*49*) and the method of Fushman et al. (*50*) were used to calculate initial estimates of the correlation time. For these calculations, experimental T_1/T_2 ratios that were more than one standard deviation above or below the average were removed. Both methods yielded similar results for the global correlation time with an average estimate of 9.7 ± 0.4 ns.

The SMF equation (eq 9) applies to a molecule undergoing isotropic tumbling in solution. Modifications to the SMF equation for axially symmetric as well as fully asymmetric molecules have been described (*51, 52*). However, the Lipari−Szabo mapping technique used here requires the simplified isotropic tumbling formalism. Thus, the diffusion tensor macro r2r1_diffusion (Dr. Arthur Palmer, Columbia University) was used to assess whether P protein is more appropriately described by spherical or axially symmetric tumbling and to calculate the extent of rotational anisotropy. Using the crystal structure of the *B. subtilis* P protein (pdb code 1A6F, (*53*)), the anisotropy factor (defined as the ratio of the diffusion constants parallel ($D_\parallel$) to the long axis of the molecule over the diffusion constants perpendicular ($D_\perp$) to that axis) was calculated to be 1.20 ± 0.01, which is slightly aspherical. Additionally, the axially symmetric model does provide a small statistically significant improvement to the best fit of the R_2/R_1 ratios compared to the spherical model (reduced χ^2 value of 5.85 versus 8.96). However, the correlation times derived from these two models are equivalent within error, $\tau_m^{iso} = 9.748 \pm 0.018$ ns and $\tau_m^{eff} = 9.716 \pm 0.022$ ns. Furthermore, theoretical (*48*) and experimental (*51, 54*) studies have demonstrated that there is not a significant change in calculated SMF parameters (S^2 and τ_e) for cases of slight ($D_\parallel/D_\perp \leq 1.35$) and even moderate ($D_\parallel/D_\perp \leq 2.0$) anisotropy. Therefore, the relaxation data was analyzed using the SMF equation (eq 9) with a single isotropic correlation time (τ_m^{iso}) of 9.7 ns. A variation in the correlation time of 0.1 ns does not significantly affect the predicted S^2 and τ_e using the Lipari−Szabo mapping method (data not shown).

As an example, Figure 3A displays the application of the Lipari−Szabo mapping technique (*28*) to determine the order parameter (S^2) and internal correlation times (τ_e) for the backbone amide groups of Q69 (α-helix 2) and K119 (the C-terminus). This analysis is based on the comparison of the experimentally determined high-frequency spectral densities, $J(0.87\omega_H)^{obs}$ and $J(\omega_N)^{obs}$, to those predicted for an internally rigid, isotropic tumbling protein denoted as $J(0.87\omega_H)^{rigid}$ and $J(\omega_N)^{rigid}$. Under the limits of no (or extremely fast) internal motions ($\tau_e \rightarrow 0$) and absolute amide NH bond rigidity ($S^2 = 1$), the model-free spectral density function of eq 9 is simplified to one term:

$$J(\omega_i)^{rigid} = (2/5)[\tau_m/(1 + (\omega_i\tau_m)^2)] \tag{10}$$

The predicted spectral densities at the angular frequencies $0.87\omega_H$ and ω_N for a rigidly tumbling molecule can be calculated at any given correlation time (τ_m); this yields a unique $\{J(\omega_N)^{rigid}, J(0.87\omega_H)^{rigid}\}$ pair per τ_m. The "Lipari−Szabo map" or "rigid tumbling curve" is then a continuous line composed of $\{J(\omega_N)^{rigid}, J(0.87\omega_H)^{rigid}\}$ points plotted in *x-y* coordinate space ($0 \leq \tau_m \leq 50$ ns is shown in Figure 3A). The triangular-shaped rigid tumbling curve has top and right-hand vertices that correspond to the correlation times that maximize $J(\omega_i)^{rigid}$ at $(0.87\omega_H)^{-1}$ (i.e., 305 ps) and $(\omega_N)^{-1}$ (i.e., 2.619 ns) respectively. The point on the rigid tumbling curve corresponding to the calculated correlation time for P protein (9.7 ns) is highlighted as a blue square in Figure 3A and is denoted as $\{J(\omega_N)^{\tau_m}, J(0.87\omega_H)^{\tau_m}\}$. Any backbone ^{15}N on P protein that lacks internal amide NH bond vector motions and is completely rigid should overlap with $\{J(\omega_N)^{\tau_m}, J(0.87\omega_H)^{\tau_m}\}$. The presence of fast internal motions ($S^2 \neq 1$, $\tau_e \neq 0$) is observed as a shift away from the $\{J(\omega_N)^{\tau_m}, J(0.87\omega_H)^{\tau_m}\}$ point into the space within the triangle, as is the case for Q69 and K119. A line can be drawn from the $\{J(\omega_N)^{\tau_m}, J(0.87\omega_H)^{\tau_m}\}$ point *through* the $\{J(\omega_N)^{obs}, J(0.87\omega_H)^{obs}\}$ point for a given amide to another point on the rigid tumbling curve. This other point is the $\{J(\omega_N)^{\tau}, J(0.87\omega_H)^{\tau}\}$ pair that corresponds to the reduced spectral densities that would be predicted from the model-free equation (eq 9) if ^{15}N relaxation was solely caused by fast internal motions ($S^2 = 0$) with an effective correlation time of τ. The effective correlation times for Q69 and K119 are 27.9 and 127.7 ps respectively, which gives internal correlation times (τ_e's) of 28.0 and 129.4 ps. The line segments shown in Figure 3A depict eq 9 with S^2 varying from 1 (τ_m endpoint on the rigid tumbling curve) to 0 (τ endpoint). Thus, S^2 is given by the fraction defined by the distance of the observed point to the τ point over the distance from the τ_m point to the τ point:

$$S^2 = \frac{[\{J(\omega_N)^{obs} - J(\omega_N)^{\tau}\}^2 + \{J(0.87\omega_H)^{obs} - J(0.87\omega_H)^{\tau}\}^2]^{1/2}}{[\{J(\omega_N)^{\tau_m} - J(\omega_N)^{\tau}\}^2 + \{J(0.87\omega_H)^{\tau_m} - J(0.87\omega_H)^{\tau}\}^2]^{1/2}} \tag{11}$$

The order parameters for Q69 and K119 determined using this approach are 0.92 ± 0.03 and 0.35 ± 0.02. The errors from the observed spectral densities, $J(\omega_N)^{obs}$ and $J(0.87\omega_H)^{obs}$, were propagated to calculate the uncertainty of S^2.

We have explored the effect of reduced spectral density error on the calculation of S^2 and τ_e to determine the robustness of the Lipari−Szabo mapping technique. The error for the experimental $J(0.87\omega_H)$ and $J(\omega_N)$ values of Q69 and K119 are shown in Figure 3A. The resulting scope of plausible τ's for both Q69 and K119 were calculated. The τ's appear to be well determined for K119 (115 ps ≤ τ ≤ 143 ps) while there is significant uncertainty in the internal correlation time for Q69 (17.4 ps ≤ τ ≤ 428 ps). Since most of the observed $\{J(\omega_N)^{obs}, J(0.87\omega_H)^{obs}\}$ points cluster around

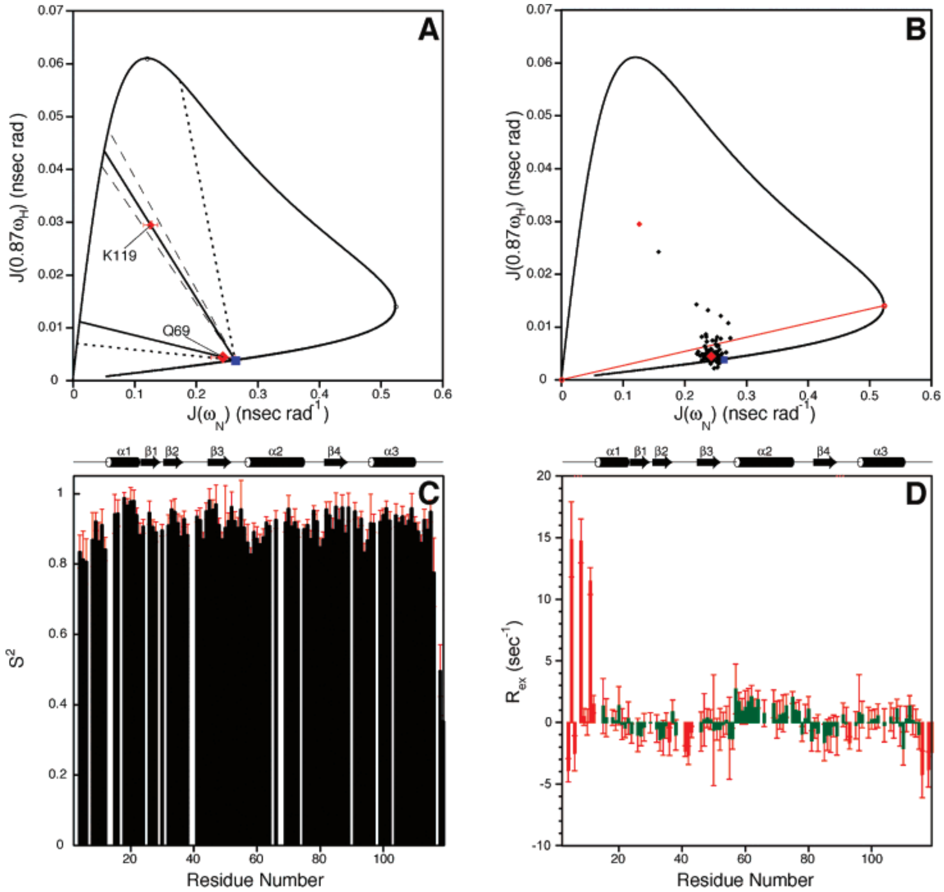

FIGURE 3: Application of the Lipari−Szabo mapping method (*28*) to P protein: extracting simple model free (SMF) parameters S^2, τ_e, and R_{ex} from the reduced spectral densities $J(0.87\omega_H)$ and $J(\omega_N)$ (see text). (A) The application of the Lipari−Szabo mapping method is shown for Q69 and K119, represented as red diamonds with their standard errors. The blue square is the predicted $\{J(\omega_N), J(0.87\omega_H)\}$ pair at the global tumbling rate for P protein (9.7 ns), $\{J(\omega_N)^{\tau_m}, J(0.87\omega_H)^{\tau_m}\}$. The order parameters for Q69 and K119 are 0.918 and 0.353 with corresponding τ_e's of 28 and 129.4 ps respectively. The ranges of possible τ_e values for Q69 and K119 are determined using the dotted and dashed lines that pass through the lower left and upper right corners of the rectangle defined by the error bars around each $J(0.87\omega_H)$ and $J(\omega_N)$ point. These ranges are 17.5 ps $\leq \tau_e \leq$ 448 ps for Q69 and 116 ps $\leq \tau_e \leq$ 146 ps for K119. (B) All of the data plotted onto the Lipari−Szabo map. The red diamonds and the blue square are the same as in (A). Most of the resonances cluster around the Q69 point. Sixteen residues have points above the red line. The procedure described in the text provides accurate estimates of τ_e for points above this line, whereas experimental error precludes accurate determination of τ_e for points below the line. Error bars have been omitted from this plot for clarity but can be found in Figure 2A and 2B. The points outside the rigid tumbling curve are within experimental error of the line. (C) The order parameters calculated using eq 11 and (D) the chemical exchange contribution to R_2 (i.e., R_{ex}) from the simplified model-free Lipari−Szabo mapping method are displayed for the entire P protein sequence. Note: $J(0)^m$ is given by eq 14 for most of the data (green bars), except for the sixteen residues with reliable τ_e's (red bars) which required eq 15.

the Q69 point on the Lipari−Szabo map (Figure 3B), the internal correlation times for most of the amides are not reported. Thus, the Lipari−Szabo map provides a simple graphical means to understand the source of the ambiguity of τ_e at high S^2. On the other hand, the variability in S^2 as determined by Lipari−Szabo mapping is not significant for amides that contain either high (Q69) or low (K119) order parameters. Therefore, the error in S^2 was derived from the propagated errors through eq 11 using standard techniques (*40*).

The order parameters for all of the 99 well-resolved amide cross peaks were determined using eq 11, and the results from this SMF analysis are shown in Figure 3C (see Table S4, Supporting Information, for the corresponding data). The observed S^2 values are relatively high and uniform across the entire sequence. The average S^2 over the entire sequence is 0.902 ± 0.081 with an average error for the calculated order parameters of ~2%. The three C-terminal residues are the only backbone nitrogens that have an S^2 below 0.8, which most likely reflects the high mobility of the apparently disordered C-terminal tail of P protein. In contrast, the N-terminus, including residues L4−K12, has order parameters above 0.8 suggesting the lack of flexibility on the ps−ns time scale for this portion of P protein. This observation is relatively surprising (and deceiving) in light of the evidence for conformational heterogeneity (i.e., μs−ms motions) in this region (see below).

Determination of R_{ex}, the Chemical Exchange Contribution to R_2, from J(0). The presence of conformational fluctuations on the μs−ms time scale can cause transverse relaxation rates to be higher than would be measured in the absence of these motions. This increment to R_2 is known as R_{ex}, or the chemical exchange contribution to R_2, and is treated as the residual of the measured R_2 (R_2^{obs}) that cannot be attributed to global tumbling and fast internal motions alone (R_2^{m}) (*55*):

$$R_2^{obs} = R_2^{m} + R_{ex} \tag{12}$$

Since $J(0)$ is the only reduced spectral density that contains a contribution from R_2, a simple expression describing the contribution of molecular tumbling to R_2 ($R_2{}^{m}$) can be determined through the inversion of eq 8:

$$R_2{}^{m} = J(0)^{m}(d^2/2 + 2c^2/3) + J(\omega_N)^{obs}(3d^2/8 + c^2) + J(0.87\omega_H)^{obs}(13d^2/8) \quad (13)$$

where $J(0)^{m}$ is the predicted zero frequency spectral density in the absence of conformational exchange; $J(\omega_N)^{obs}$ and $J(0.87\omega_H)^{obs}$ are the observed high-frequency reduced spectral densities for a given backbone amide NH bond (Table S3). $J(0)^{m}$ can be estimated from $J(\omega_N)^{obs}$ and τ_m under the assumptions that (i) eq 9 provides an adequate description of the spectral density function and that (ii) fast internal motions are very rapid ($\tau_e \leq 100$ ps). If these assumptions hold, $J(0)^{m}$ is given by

$$J(0)^{m} = J(\omega_N)^{obs}[1 + (\omega_N\tau_m)^2] \quad (14)$$

Alternatively, $J(0)^{m}$ can be determined directly from the best-fit parameters (S^2 and τ) obtained from the SMF analysis (eq 9):

$$J(0)^{m} = (2/5)[S^2\tau_m + (1 - S^2)\tau] \quad (15)$$

Given the high degree of uncertainty for τ (τ_e) for most of the data (Figure 3B), eq 14 was used to approximate $J(0)^{m}$. However, when the observed $\{J(\omega_N)^{obs}, J(0.87\omega_H)^{obs}\}$ point is significantly displaced from the $\{J(\omega_N)^{\tau_m}, J(0.87\omega_H)^{\tau_m}\}$ point, the internal correlation times are better defined (see K119 in Figure 3A) and eq 15 is the more appropriate equation to estimate $J(0)^{m}$. Therefore, a cutoff line between the origin and the point on the rigid tumbling curve with the highest $J(\omega_N)$ (red line in Figure 3B) is drawn to delineate the backbone amide nitrogens whose Lipari−Szabo mapping points are sufficiently displaced from the rigid, global tumbling point to determine reliable τ's. There are 16 such residues, and they reside within the N-terminal region (L4−K6, N8−K12), the C-terminus (S116, S118, and K119), the metal-binding loop (L36, N41−E43) and the β4−α3 linker (Q93).

R_{ex} was calculated using this semiquantitative method (eqs 12−15), and the data are displayed in Figure 3D. The average R_{ex} for the residues processed using eq 14 is 0.13 ± 0.99 s^{-1}. Thus, the relaxation data for most of P protein can be modeled using the SMF analysis where fast internal motions are not significant (i.e., $\tau_e \leq 100$ ps). Residues with clearly broadened lines were not included in this average. The R_{ex} values for the 16 amides that are sufficiently displaced from the global tumbling Lipari−Szabo map point (i.e., required eq 15) are displayed as red bars in Figure 3D. Three residues within the N-terminal region (K5, N8, K11) have a statistically significant R_{ex} value. However, ten residues (L4, K6, L36, N41, D42, E43, Q93, S116, S118, and K119) have implausible negative R_{ex} values suggesting that the SMF formalism (eq 9) is not an adequate model of the ps−ns motions that give rise to ^{15}N relaxation for these residues. Note the exclusion of fast internal motions in the calculation of $J(0)^{m}$ for these residues (i.e., using eq14 instead of eq15) would result in even lower (more negative) estimates for R_{ex}. It is common in this circumstance to apply the "extended model-free" formalism to determine order parameters for two different time scale internal motions (*46*).

Incorporation of Extended Model-Free Formalism into Lipari−Szabo Mapping Analysis. The spectral density function for the "extended model-free" (EMF) formalism contains three principal terms:

$$J(\omega) = \frac{2}{5}\left[\frac{S^2\tau_m}{1 + (\omega\tau_m)^2} + \frac{(1 - S_f{}^2)\tau_f{}'}{1 + (\omega\tau_f{}')^2} + \frac{(S_f{}^2 - S^2)\tau_s{}'}{1 + (\omega\tau_s{}')^2}\right] \quad (16)$$

The effective correlation times $\tau_f{}'$ and $\tau_s{}'$ are related to two internal correlation times τ_f and τ_s through the relationship $(\tau_i{}')^{-1} = (\tau_i)^{-1} + (\tau_m)^{-1}$ where i is either f or s. Note that the global tumbling rate is slower than both internal motion time constants τ_f and τ_s. The order parameters for these fast internal motions are defined as $S_f{}^2$ and $S_s{}^2$ respectively; and if it is assumed that the two fast internal motions are independent of each other, then the overall order parameter S^2 is defined as the product $S_f{}^2S_s{}^2$ (*46*). If it is assumed that τ_f is extremely fast (i.e., τ_f, $\tau_f{}' \rightarrow 0$), eq 16 reduces to

$$J(\omega) = \frac{2}{5}\left[\frac{S^2\tau_m}{1 + (\omega\tau_m)^2} + \frac{(S_f{}^2 - S^2)\tau_s{}'}{1 + (\omega\tau_s{}')^2}\right] = \frac{2S_f{}^2}{5}\left[\frac{S_s{}^2\tau_m}{1 + (\omega\tau_m)^2} + \frac{(1 - S_s{}^2)\tau_s{}'}{1 + (\omega\tau_s{}')^2}\right] \quad (17)$$

Thus in this limit, the EMF equation has a similar mathematical form to the SMF equation (see eq 9). Indeed, the two expressions are equivalent when $S_f{}^2$ is unity. Furthermore, $S_s{}^2$ and $\tau_s{}'$ (eq 17) are analogous to S^2 and τ_e (eq 9), and $S_f{}^2$ can be considered an additional scaling factor.

Although the SMF analysis is insufficient to properly describe the relaxation data of the ten residues listed above, the EMF analysis suffers from adding an additional parameter without adding any more data. As discussed below, it is possible to identify a range of values for the order parameter of an additional mode of internal motion ($S_f{}^2$). This range of values produces a corresponding range of $J(0)^{m}$ values, which in turn results in a range of R_{ex} values. In our opinion, this is the most valid application of EMF to our data and although results are presented as ranges, they nevertheless provide useful information. Briefly described below is the implementation of Lipari−Szabo mapping for EMF analysis and the way to obtain estimated ranges for $S_f{}^2$ as originally illustrated by Andrec et al. (see Figure 5 and associated text in (*28*) for greater detail).

An example of EMF analysis via Lipari−Szabo mapping is shown in Figure 4A for Lys 6 data. The two terms of eq 17 can be represented on the Lipari−Szabo map as two corresponding lines. The first line (blue), representing the fast time scale internal motion, connects the origin ($\tau_f{}' \rightarrow 0$ on the rigid tumbling curve) to $J(\omega_N)^{obs}$, $J(0.87\omega_H)^{obs}$ and extends to the other side of the rigid tumbling curve. The second line (green) describes the slower internal motion and connects the $\{J(\omega_N)^{\tau_m}, J(0.87\omega_H)^{\tau_m}\}$ point on the rigid tumbling curve, through $\{J(\omega_N)^{obs}, J(0.87\omega_H)^{obs}\}$ to the point on the other side of the rigid tumbling curve. This is the same line used in the SMF method described above.

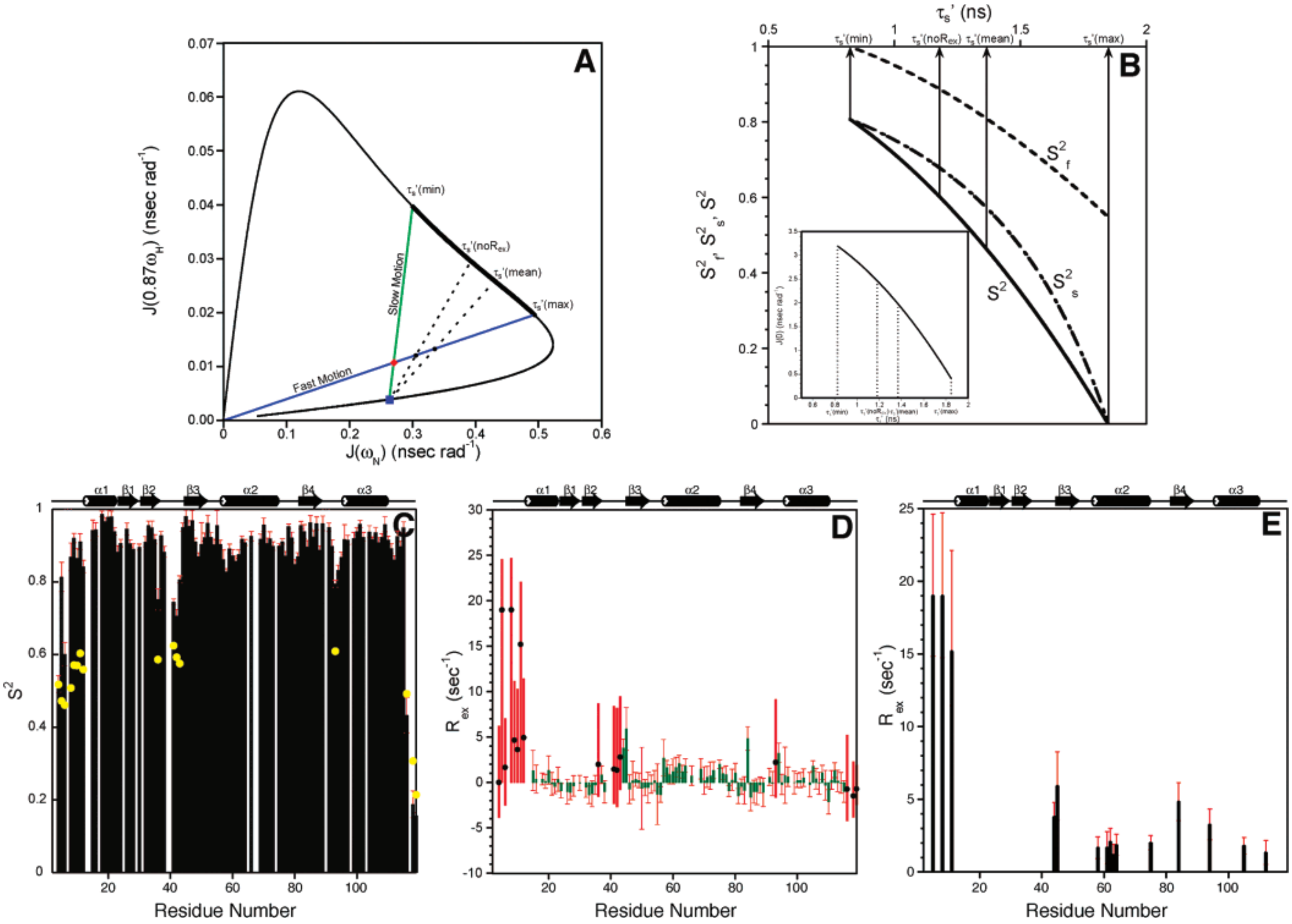

FIGURE 4: Incorporation of the extended model-free (EMF) formalism within the Lipari−Szabo mapping method: reanalysis of sixteen residues containing substantial fast internal motions (see text). (A) Application of the EMF formalism for the example Lys6. The Lipari−Szabo points corresponding to global tumbling and K6 are represented as a blue square and a red diamond. The solid lines through the K6 point represent the fast (blue) and slow (green) motion terms in eq 17. As described in the text, the intersections of these lines with the solid black rigid tumbling curve give the limits for the range of possible τ_s' values that are consistent with the observed K6 $\{J(\omega_N),J(0.87\omega_H)\}$ under the EMF model. This range is given by $\tau_s'(\text{min}) \leq \tau_s' \leq \tau_s'(\text{max})$ and depicted on the rigid tumbling curve as a thicker line. Within these limits $1 \geq S_f^2 \geq S_f^2(\text{min})$ and $S_s^2(\text{max}) \geq S_s^2 \geq 0$. For K6, 823.9 ps $\leq \tau_s' \leq$ 1.849 ns, $1 \geq S_f^2 \geq 0.548$, and $0.808 \geq S_s^2 \geq 0$. Shown in dashes are the mapping lines for $\tau_s'(\text{no}R_{ex})$ and $\tau_s'(\text{mean})$ (see text). (B) The effect of increasing τ_s' from $\tau_s'(\text{min})$ to $\tau_s'(\text{max})$ on the EMF parameters S_f^2, S_s^2, S^2, and the corresponding $J(0)^m$ values (inset). (C) The S^2 values derived from the EMF analysis for the sixteen residues that may have substantial fast internal motions are displayed with yellow circles. The displayed upper limit of S^2 is defined by one of two conditions: (i) $S^2(\text{max})$ when $R_2^{obs} > R_2^m$ for all τ_s'; this is true for K5, N8, R9, L10, K11, and K12; and (ii) $S^2(\text{no}R_{ex})$, when τ_s' results in $R_2^{obs} = R_2^m$; this is the value given for the other ten EMF-analyzed residues (L4, K6, L36, N41, D42, E43, E93, S116, S118, and K119). The solutions to the EMF equation at $\tau_s' = \tau_s'(\text{mean})$ are also shown as yellow circles. (D) The corresponding range of R_{ex} values using the color scheme as in Figure 3D. The calculated R_{ex} values reflecting the EMF solution at $\tau_s'(\text{mean})$ are shown as black circles. The rest of the protein sequence, which was analyzed using the SMF formalism, is shown as green bars. (E) The residues that display a statistically significant R_{ex} are displayed as a function of the protein sequence. In the present study, "statistically significant" is defined by the following condition: $R_{ex} - 1.5\sigma \geq 0$. The displayed errors reflect either (1) the propagated standard error calculated for those residues analyzed by the SMF equation or (2) the entire plausible range in R_{ex} obtained from the EMF analysis. The secondary structure of P protein is shown for (C), (D), and (E).

The intersections of these two lines with the rigid tumbling curves define the range of possible τ_s' values for EMF analysis. The intersection of the fast motion line with the rigid tumbling curve defines $\tau_s'(\text{max})$, where the minimum value of S_f^2 in the EMF analysis would apply. $S_f^2(\text{min})$ can be determined from the ratio

$$S_f^2(\text{min}) = \frac{J(\omega_N)^{obs}}{J(\omega_N)^{\tau_{max}}} = \frac{J(0.87\omega_H)^{obs}}{J(0.87\omega_H)^{\tau_{max}}} \qquad (18)$$

For K6, $\tau_s'(\text{max})$ is 1.849 ns and $S_f^2(\text{min})$ is 0.548. Note that $\tau_s'(\text{max})$ and $S_f^2(\text{min})$ do not depend on $\{J(\omega_N)^{\tau_m}, J(0.87\omega_H)^{\tau_m}\}$. The rigid tumbling curve intersection of the slow motion line corresponds to $\tau_s'(\text{min})$, where no internal fast motion occurs ($S_f^2 = 1$.) In Figure 4A, $\tau_s'(\text{min})$ for K6 is 823.9 ps and S_s^2, or $S^2(\text{max})$, is 0.808 as calculated from eq 11. The region between these two lines on the rigid tumbling curve (thicker in Figure 4A) represents all possible values of τ_s', each of which has a corresponding value of S_f^2 and S_s^2. As τ_s' increases from $\tau_s'(\text{min})$ to $\tau_s'(\text{max})$, the intersection point of the two lines moves away from $\{J(\omega_N)^{obs}, J(0.87\omega_H)^{obs}\}$ and goes to $\{J(\omega_N)^{\tau_{max}}, J(0.87\omega_H)^{\tau_{max}}\}$ (Figure 4A). Therefore, the τ_s', S_f^2 and S_s^2 values corresponding to *any* point on the fast motion line between $\{J(\omega_N)^{obs}, J(0.87\omega_H)^{obs}\}$ and $\{J(\omega_N)^{\tau_{max}}, J(0.87\omega_H)^{\tau_{max}}\}$ are equally consistent with the observed high-frequency spectral densities. This ambiguity is the result of attempting to fit the four parameter EMF model to three experimental observations. For this reason, we focus here on the limits of possible values for S^2 and R_{ex} for the sixteen residues analyzed by the EMF model.

The order parameters corresponding to this range of possible τ_s' values are plotted in Figure 4B. As τ_s' increases from its minimal value, S_f^2 and S_s^2 decrease from their maximum values of 1 and S_s^2(max) to S_f^2(min) and 0 respectively. This results in a dramatic change in S^2 as a function of τ_s'. This large range of possible internal motion order parameters gives rise to a range of possible $J(0)^m$ values (eq 17): from 3.20 ns/rad at τ_s'(min) to 0.40 ns/rad at τ_s'(max) (Figure 4B, inset). This variation in $J(0)^m$, in turn, leads to a similar nonlinear monotonic decrease in R_2^m (eq 13) and thus an *increase* in apparent R_{ex} (eq 12). Two arbitrary intermediate τ_s' values are depicted in Figures 4A and 4B. One point, τ_s'(noR_{ex}), corresponds to the condition when τ_s', S^2, and S_f^2 yield a calculated R_{ex} of zero. For K6, this occurs when τ_s' is 1.181 ns and the fast internal and overall order parameters (S_f^2 and S^2) are 0.887 and 0.601 respectively. As an alternative to assuming that R_{ex} is 0, we propose another equally valid intermediate τ_s' point, τ_s'(mean), which represents the τ_s' value that yields a $J(0)^m$ value in the middle of range of $J(0)^m$ values defined by τ_s'(min) and τ_s'(max). The τ_s'(mean) for K6 is 1.367 ns with an S_f^2 and S^2 of 0.808 and 0.461 respectively. For this value of τ_s', R_{ex} is 1.68 s^{-1}. We propose that the R_{ex} calculated from $\tau_s' = \tau_s'$(mean) is reasonable to use as the middle of the R_{ex} range for the sixteen residues analyzed by EMF.

Figures 4C and 4D display the results of the EMF analysis for the sixteen chosen residues in combination with the rest of the protein, which was adequately fit by the SMF model. The inclusion of the EMF analysis drastically changes the interpretation of the fast internal dynamics of P protein, specifically at the N-terminal region (L4−K12) and the metal-binding loop (L36, N41−E43). Although the EMF analysis permits a wide range of feasible S^2 values ($0 \leq S^2 \leq S^2$(noR_{ex})), the new interpretation indicates more fast time scale motion than was apparent using SMF analysis. At the N-terminus, the upper limit for the S^2 values of L4 and K6 are ~0.5−0.6 which is more typical of a disordered structure than an internally rigid one. Although the upper limit of S^2 does not formally change for the other N-terminal residues, K5 and N8−K12 (as $R_2^m(\max) \leq R_2^{obs}$), it is likely that these residues also have depressed order parameters as suggested by the S^2(mean) for these sites. Lower S^2 values would be consistent with the elevated $J(0.87\omega_H)$ values and depressed $^{15}N\{^1H\}$-NOEs found for this region (Figures 1C and 2A), all of which suggest the presence of significant fast internal motions. Indications for internal flexibility are also found within the metal-binding loop because the upper limit S^2(noR_{ex}) drops below 0.8 for L36, N41, and D42.

The inclusion of the second fast internal time scale in the EMF analysis corrects the nonphysical negative R_{ex} values that result from the SMF analysis (compare Figure 4D with Figure 3D). Furthermore, the EMF analysis provides a range of possible positive R_{ex} values as τ_s' varies from τ_s'(min) to τ_s'(max). R_{ex} values can be altered by 10 s^{-1} in some cases when the possible τ_s' range is large. Using the τ_s'(mean) point to define the best-fit EMF conditions, the N-terminal region (L4−K12), the metal-binding loop (L36, N41−K45), and the β4−α3 linker (Q93−L94) all appear to undergo motions on the slow μs−ms time scale. However, τ_s'(noR_{ex}) also provides an adequate alternative solution using the EMF analysis. Thus, the residues whose ^{15}N relaxation data can be modeled equally well under both τ_s' conditions were excluded from the list of residues that contain a statistically significant R_{ex}.

Figure 4E displays the residues that unambiguously exhibit R_{ex} (see Table S4, Supporting Information). These residues map onto specific regions of P protein (see Discussion): K5, N8, K11 (N-terminal region); L44 and R45 (the β2−β3 linker, termed the metal-binding loop,); V58, N61−K64 (the N-terminal portion of α-helix 2, part of the RNR motif); K75 (α2−β4 linker); I84 (β-strand 4); L94 (β4−α3 linker); H105 (α-helix 3); and L112 (C-terminal region).

DISCUSSION

Sulfate-Refolded P Protein Is Rigid throughout Most of the Structure. The two model-free parameters that describe the fast internal motions of an amide NH bond vector on an isotropically tumbling protein are the order parameter, S^2, and the internal correlation time τ_e (or τ_s using the EMF model). For most of P protein, the SMF model explains the data but τ_e cannot be accurately determined; thus, the observed ^{15}N relaxation data yielded only the global correlation time, τ_m, and S^2. The average order parameter for P protein, excluding the sixteen residues that required the EMF analysis, is 0.919 ± 0.035. The sixteen EMF-analyzed residues, which reside at the protein termini and the metal-binding loop, were not included in this average because S^2 cannot be precisely determined at those sites (see below). The high S^2 obtained for the rest of the protein suggests that ligand-folded P protein has only limited internal dynamics on the ps−ns time scale. The average order parameter of P protein is slightly higher than the averaged S^2 of 0.84 ± 0.11 reported for 20 proteins (*54*). The lack of fast internal dynamics for most of the P protein sequence may reflect a greater-than-average inflexibility for P protein. Although the potential imprecision in the reduced spectral densities, $J(0.87\omega_H)$ and $J(\omega_N)$, may artificially raise the average S^2 (*28*), the Lipari−Szabo mapping technique has been shown to yield similar model-free parameters to those obtained from the traditional statistical model-free approach (*28*, *47*). Thus, the apparent elevated S^2 values for sulfate-liganded P protein probably reflect a particular internal rigidity of this protein in solution.

The Terminal Regions, the Metal-Binding Loop, and N-Terminal Half of the RNR Motif Display Distinctive Internal Dynamics over Various Time Scales. Although most of the P protein sequence has limited internal dynamics, there are four small contiguous segments that exhibit protein fluctuations on either the fast (ps−ns) or the slow (μs−ms) time regimes, or both. These four regions are the N-terminal region (L4−K12), the metal-binding loop (L36−L44), the RNR motif (K52−R68), and the C-terminus. The residues that have order parameters below 0.8, which is commonly used as the arbitrary cutoff to distinguish “rigid” and “flexible” or “disordered” structures, are shown as red ribbon in Figure 5. Additionally, residues that exhibit unambiguously nonzero R_{ex} indicating slow conformational transitions on the μs−ms time scale are mapped onto the structure in Figure 6A. The ^{15}N dynamics of each of these segments is discussed in more detail below.

FIGURE 5: The regions of fast (ps−ns) internal motions are mapped onto the crystal structure of P protein (pdb file 1A6F (*53*)). Order parameters, S^2, above and below 0.8 are colored in green and red respectively. The former represents the "rigid" structure while the latter is described as "flexible". The yellow regions correspond to the EMF modeled residues that have a S^2(max) above 0.8 and a S^2(mean) below 0.8; both solutions are equally adequate. Furthermore, yellow regions have other signatures of fast internal motions such as depressed ^{15}N{^{1}H}-NOEs and elevated $J(0.87\omega_H)$ values (see Figures 1C and 2A). The residues that do not have chemical shift assignments are in gray (A2, H3, R7, N13, and E14). The sulfate ion observed in the crystal structure, and the coordinating side chains, are shown in blue. Note, the last five residues, K115−S119, did not have any observable electron density in the final model and therefore are not present in the crystal structure (*53*).

No electron density was observed for the last five residues in the crystal structure of *B. subtilis* P protein (*53*), suggesting that this portion of the protein may also be disordered in solution. Consistent with this supposition, we find that the C-terminus has the characteristics of a disordered peptide from S116 to K119. Specifically, the upper limit of S^2 in this region ranges from 0.16 to 0.43 and reflects the elevated high-frequency motions that are revealed by the elevated $J(0.87\omega_H)$ and the low (or negative) ^{15}N{^{1}H}-NOEs.

The RNR motif is an approximately 18-residue region corresponding to the most conserved sequence among bacterial P proteins (*56*), whose consensus is K-X$_{4-5}$-A-X$_2$-R-N−X$_2$-(K/R)-R-X$_2$-(R/K). In the crystal structure, this conserved motif encompasses the N-terminal half of α-helix 2 and its preceding loop, which begins the unusual left-handed crossover between the parallel β-strands 3 and 4 (*53*). The possible functional importance of the RNR motif is amplified by the fact that this unusual topology (*57*) has been maintained through evolution. However, the precise function of this motif in RNase P holoenzyme assembly, pre-tRNA binding, and/or the catalytic cycle, has yet to be elucidated. Here, our results reveal that the central portion of this motif, V58, N61−K64, exhibits statistically significant motions on the slow (μs−ms) time scale (Figure 4E).

The metal-binding loop is a relatively long loop, L36−L44, that connects β-strands 2 and 3 of the central β-sheet. This linker region has an unusually high density of acidic residues, and it coordinates one of the two Zn^{2+} atoms found in the *B. subtilis* crystal structure (*53*). Given the recent evidence that P protein enhances the affinity of at least four Mg^{2+} atoms within the substrate-bound holoenzyme complex (*24*), the metal-binding loop may serve as the conduit for this critical function. However, it should be noted that, under the conditions of the experiments described here, we have no evidence that the metal binding loop is occupied because divalent cations were not included in the buffer. As shown in Figure 4D, the upper limit for the order parameter ranges from 0.707 to 0.807 for four residues in this region (L36, N41−D43) indicating that they have increased flexibility on the ps−ns time scale. All of these residues were analyzed using the EMF equation (see Figure 4A), which assumes no information about chemical exchange (e.g., $R_{ex} = 0$). The EMF model is unable to resolve whether these residues have

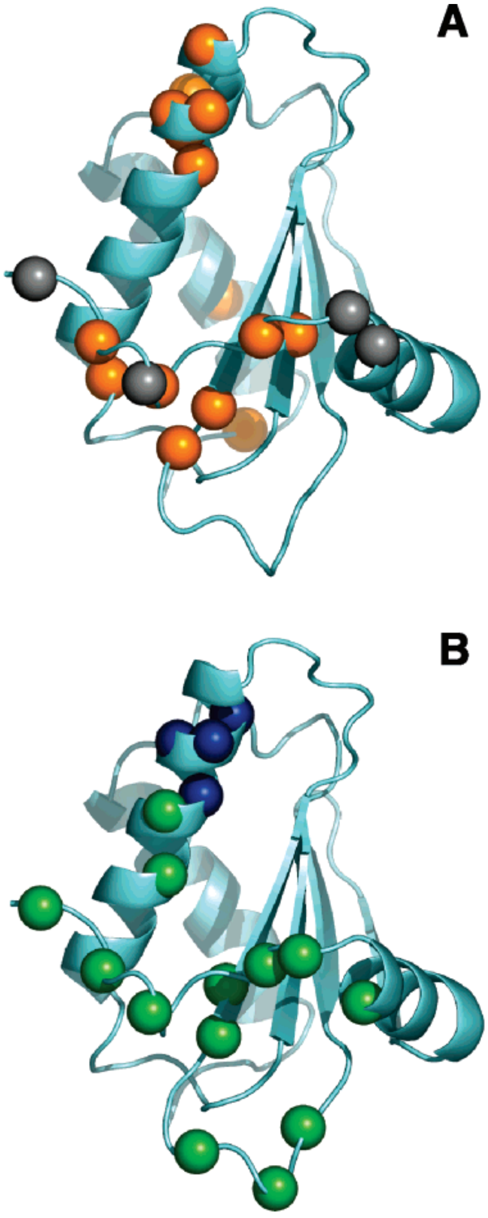

FIGURE 6: (A) The regions of slow (μs−ms) internal motions, or conformational heterogeneity, are mapped onto the P protein crystal structure. The backbone amide nitrogens that display a statistically significant R_{ex} are shown as orange spheres (see Figure 4E). Additionally, the residues that are missing in the HSQC (H3, R7, N13, E14) are shown as gray spheres; it is assumed that these residues are absent due to extreme line broadening. (B) The sites that interact with P RNA based on the hydroxyl-radical cleavage assays from Fierke and co-workers (*81*) are shown in green. The sites that interact with both P RNA and pre-tRNA are in blue.

both chemical exchange and motions on two fast internal time scales (τ_s and τ_f). Any S^2 within the range $0 \leq S^2 \leq S^2(\text{no}R_{ex})$ is an *equally plausible* estimate for S^2 and thus S_f^2; this leads to a corresponding range of possible R_{ex} values (Figure 4D). The potential R_{ex} range for these residues is 0 $s^{-1} \leq R_{ex} \leq 8.7\ s^{-1}$, where R_{ex}(mean) (i.e., the average R_{ex} value when evaluated at τ_s'(mean)) is ~1.9 s^{-1} over all four amino acids (see Results). However, because these residues may have no R_{ex}, they are not highlighted in Figure 6A. Dispersion experiments (*58*−*60*) are required to independently determine an estimate of R_{ex} in order to confine the plausible range of S^2 and S_f^2 for those residues that required the EMF analysis.

The N-terminal region, A2−K12, is a highly basic stretch containing seven H, K, or R residues and no corresponding D or E residues. In the crystal structure this stretch of sequence has no regular secondary structure and covers one edge of the central β-sheet before turning sharply to α-helix 1, which covers the sheet face (*53*). The ^{15}N relaxation dynamics suggest that this region is mobile over both the ps−ns and μs−ms time scales, based on the following evidence. Conformational heterogeneity on the μs−ms time scale is evident from the large R_{ex} values observed for K5, N8, and K11 (Figure 4E). Furthermore, four additional residues within the first 13 residues (H3, R7, N13, and D14) are not seen in the HSQC. These peaks are likely missing because of extreme line broadening caused by dynamics on this slower μs−ms time scale. The N-terminal region also has fast internal motions on the (ps−ns) time scale indicated by low order parameters for L4 and K6 (<0.52 and 0.60 respectively.) The order parameters for the other residues in the N-terminus, K5 and N8−K12, are likely to be lower than the S^2(max) values shown in Figure 4E because these resonances have similarly low ^{15}N{^{1}H}-NOEs, elevated $J(0.87\omega_H)$, and *plausible* S^2(mean) values similar to L4 and K6. As with the metal-binding loop, reduction of the order parameter from the upper limits, S^2(max) or $S^2(\text{no}R_{ex})$, would result in an increase in the corresponding R_{ex} as displayed in Figure 4E. Thus, dispersion experiments are necessary to accurately estimate R_{ex}, and thus S^2. Overall, the data suggest that the N-terminal region fluctuates between two (or more) populated states on the μs−ms time scale whose fast internal dynamics are significant (i.e., highly flexible). Note that the interconverting conformations cannot be sulfate-bound and unbound forms because the fraction of the unbound conformation (≤0.02%) is too small to contribute significantly to R_{ex}.

Residues That Display Significant R_{ex} Reside on the Putative P RNA−P Protein Interface. Regions of conformational heterogeneity (i.e., significant R_{ex}) in the vicinity of ligand recognition surfaces have been noted in some proteins (*61*). These proteins display μs−ms motions in the absence of the binding partner that are either quenched or suppressed upon complex formation. This phenomenon has been observed for proteins that bind to peptides (*62, 63*), DNA (*64, 65*), RNA (*12*), and small molecule substrates/ligands (*58, 66*−*68*). Conformational heterogeneity has also been observed on surfaces known to mediate critical protein−protein interactions (*69, 70*). In some cases, the rates of conformational exchange (k_{ex}) are of the same magnitude as ligand binding kinetics (*58, 66, 67*). This observation suggests that the functional rates of ligand binding and/or release may be controlled by the conformational "switches" observed by NMR (*61*). Thus, the protein surfaces that demonstrate conformational heterogeneity may reveal the sites of protein interaction as well as the mechanisms responsible for that interaction. In this study, we find that the residues that have an observable R_{ex} cluster onto a specific region of P protein (Figure 6A) and there is a strong correspondence between this mapped surface and the putative P protein−P RNA holoenzyme interface (Figure 6B).

Most of the residues indicated in Figure 6A localize to a specific surface defined by the N-terminal region (K5, N8, K11), the metal-binding loop/β-strand 3 (L44, K45), and the RNR motif (V58, N61−K64). Four additional residues in the N-terminal region with missing resonances in the HSQC spectrum (H3, R7, N13, E14) are also found on this surface and included in Figure 6A. There is also the possibility of chemical exchange at other positions within the N-terminal region (L4, K6, R9, L10, K12) and the metal-binding loop (L36, N41−E43) given the range of possible S^2 for these sites (Figures 4C and 4D). However, only the residues that exhibit statistically significant chemical exchange, or are missing in the HSQC spectra, are indicated. Overall the dynamics data indicate that conformational fluctuations occur along the edge of the central β-sheet that is covered in part by the N-terminal region in the crystal structure. It is interesting to note that one of the two high affinity sulfate binding sites (*53*) is located on this surface. It is likely that this sulfate ion is displaced by RNA when the holoenzyme is formed.

Intermolecular interactions, such as dimerization or aggregation, could give rise to chemical exchange (*71*, *72*). However, sedimentation equilibrium experiments do not find evidence for monomer−dimer equilibrium under the solution conditions and protein concentration of our NMR experiments (data not shown). Additional experiments, such as ^{15}N-T_2 relaxation and/or dispersion experiments as a function of protein, may further strengthen the assertion that the observed R_{ex} arises from internal motions of the monomer.

RNase P is one of the most extensively studied ribozymes to date (see (*17*, *18*) for review), and there is a great amount known about the functional, biochemical and enzymatic aspects of RNase P. While two crystal structures of bacterial P RNA have been solved (*73*, *74*), surprisingly little is known about the structure of the holoenzyme complex. Most of the studies that probe the P RNA−P protein interface have relied on indirect assays to determine the protein sites that are important for the holoenzyme interaction. These assays, such as *in vivo* (*75*), mutagenesis (*76*), fluorescence (*77*), and EPR (*78*) studies, cannot distinguish protein sites that interact directly with the RNA from sites that are affected by a conformational change upon holoenzyme formation. Therefore, it is not surprising that these studies implicate protein sites that are distant on the protein, or even in the protein core.

More recently, an EDTA-Fe based footprinting approach has been used to characterize the protein−RNA interface (*79*, *80*). Unfortunately, this approach maps RNA sites up to 24 Å away from the backbone C_α position. Since the shortest dimension of P protein is ~30 Å (*53*), the identified protein−RNA interactions are considered "long-range" constraints (*79*). The most comprehensive study of the RNase P holoenzyme interface has been carried out by Fierke and co-workers (*81*), who use a similar directed hydroxyl-radical cleavage strategy but with a shorter tether. Single-cysteine P protein variants derivatized with acetamido-1,10-*o*-phenanthroline complexed with Cu(II) can cleave RNA sites within 10−15 Å of the protein backbone. The protein sites that gave rise to specific P RNA cleavages are shown in Figure 6B. These sites are primarily located within the N-terminal region (H3C, K5C, R7C, K11C, K12C), the metal binding loop (Q38C, E40C, D42C), and the RNR motif (R60C−R65C, R68C). Furthermore, the sites D15C (α-helix 1), R45C and V46C (β-strand 3) also map onto the same general protein surface. Additionally, their results show that the RNR motif (specifically R61C and R62C) is near the pre-tRNA cleavage site.

Comparison of Figure 6A and 6B reveals a striking correlation between the surface of P protein that exhibits conformational heterogeneity and the putative surface involved in the holoenzyme interaction. The principal exception is the metal-binding loop, where the necessity to fit the ^{15}N backbone dynamics to a model requiring two distinct fast internal motions precludes the estimation of chemical exchange in this region. Otherwise, RNase P protein appears to be another example of the empirical correlation between the μs−ms motions and protein recognition surfaces. The conformational flexibility exhibited by P protein may be important for proper holoenzyme−substrate assembly. For example, if these motions become suppressed in the holoenzyme−substrate complex, the protein adopts one particular conformation within the complex. This “induced fit” mechanism is known to be important for protein−DNA and protein−RNA interactions (*82*). Additionally, the conformational fluctuations of P protein may contribute to its function in RNase P activity. For example, one function of C5 protein is to offset the structural differences in pre-tRNA substrates to yield uniform binding and catalysis within the context of the holoenzyme (*83*). Interestingly, a recent NMR dynamics study has revealed the presence of structural plasticity in the conserved P4 region of P RNA (*84*). Thus the apparent internal motions of the proximate ribonucleoprotein components, P4 in P RNA and the RNR motif in P protein, may be important in pre-tRNA recognition.

It would be intriguing if the correlation between the observed R_{ex} surface and putative P RNA surface extends to the kinetics of chemical exchange and protein−RNA association. However, a significant amount of work is required to make such a correlation. We intend to carry out dispersion experiments (*58*−*60*) to (i) obtain a better estimate of R_{ex}, (ii) determine the time scale of exchange (*85*), and (iii) test the validity of the two-state model for the residues that display chemical exchange. An ultimate goal is to determine k_{ex} for the entire surface. This is critical in order to ascertain (i) whether the motions of the surface have the same kinetics and (ii) whether there is a correspondence between k_{ex} and the functional kinetics of RNase P holoenzyzme assembly and/or catalysis. Additionally, P protein folding/unfolding stopped-flow experiments display multiphasic kinetics (Y. C. Chang and T. G. Oas, unpublished observation). It would also be interesting to investigate the correlation between the conformational heterogeneity revealed by NMR and the multiphasic kinetics detected from different methods.

CONCLUSIONS

^{15}N relaxation experiments reveal the presence of conformational heterogeneity on the μs−ms time scale in a particular region of the structure of sulfate liganded of *B. subtilis* P protein. This region also corresponds to the putative P RNA−P protein surface. Since P protein is essential for *in vivo* activity of the RNase P holoenzyme (*19*), any information pertaining to the inherent motions of P protein may correlate to important motions involved in *B. subtilis* holoenzyme assembly and/or the catalytic cycle of the ribozyme.

ACKNOWLEDGMENT

The authors thank Drs. Ronald Venters and Shallee Page for critically reading the manuscript, and various members of the Oas laboratory for insightful discussions and advice. The authors additionally thank Dr. Venters for technical assistance with the relaxation experiments.

SUPPORTING INFORMATION AVAILABLE

Table S1 lists the conditions scanned to detect the missing peaks in the ^{15}N/^{1}H HSQC spectrum of P protein. Experimentally determined relaxation parameters ^{15}N-T_1, ^{15}N-T_2, and ^{15}N{^{1}H}-NOE for the 99 well-resolved residues are tabulated in Table S2. Table S3 lists the corresponding reduced spectral density values $J(0.87\omega_H)$, $J(\omega_N)$, and $J(0)$ derived from the relaxation parameters. Table S4 catalogues the model-free parameters S^2, S_f^2, and R_{ex} calculated using the Lipari−Szabo mapping method. This material is available free of charge via the Internet at http://pubs.acs.org.

REFERENCES

1. Leulliot, N., and Varani, G. (2001) Current topics in RNA-protein recognition: control of specificity and biological function through induced fit and conformational capture, *Biochemistry 40*, 7947−7956.
2. Weeks, K. M., and Cech, T. R. (1996) Assembly of a ribonucleoprotein catalyst by tertiary structure capture, *Science 271*, 345−348.
3. Weeks, K. M., and Cech, T. R. (1995) Protein facilitation of group I intron splicing by assembly of the catalytic core and the 5′ splice site domain, *Cell 82*, 221−230.
4. Van Gilst, M. R., Rees, W. A., Das, A., and von Hippel, P. H. (1997) Complexes of N antitermination protein of phage lambda with specific and nonspecific RNA target sites on the nascent transcript, *Biochemistry 36*, 1514−1524.
5. Mogridge, J., Legault, P., Li, J., Van Oene, M. D., Kay, L. E., and Greenblatt, J. (1998) Independent ligand-induced folding of the RNA-binding domain and two functionally distinct antitermination regions in the phage lambda N protein, *Mol. Cell 1*, 265−275.
6. Zheng, N., and Gierasch, L. M. (1997) Domain interactions in E. coli SRP: stabilization of M domain by RNA is required for effective signal sequence modulation of NG domain, *Mol. Cell 1*, 79−87.
7. Williamson, J. R. (2000) Induced fit in RNA-protein recognition, *Nat. Struct. Biol. 7*, 834−837.
8. Frankel, A. D., and Smith, C. A. (1998) Induced folding in RNA-protein recognition: more than a simple molecular handshake, *Cell 92*, 149−151.
9. Murphy, K. P., and Freire, E. (1992) Thermodynamics of structural stability and cooperative folding behavior in proteins, *Adv. Protein Chem. 43*, 313−361.
10. Palmer, A. G., 3rd, Kroenke, C. D., and Loria, J. P. (2001) Nuclear magnetic resonance methods for quantifying microsecond-to-millisecond motions in biological macromolecules, *Methods Enzymol. 339*, 204−238.

11. Korzhnev, D. M., Salvatella, X., Vendruscolo, M., Di, Nardo, A. A., Davidson, A. R., Dobson, C. M., and Kay, L. E. (2004) Low-populated folding intermediates of Fyn SH3 characterized by relaxation dispersion NMR, *Nature 430*, 586−590.
12. Mittermaier, A., Varani, L., Muhandiram, D. R., Kay, L. E., and Varani, G. (1999) Changes in side-chain and backbone dynamics identify determinants of specificity in RNA recognition by human U1A protein, *J. Mol. Biol. 294*, 967−979.
13. Gubser, C. C., and Varani, G. (1996) Structure of the polyadenylation regulatory element of the human U1A pre-mRNA 3′-untranslated region and interaction with the U1A protein, *Biochemistry 35*, 2253−2267.
14. Palmer, A. G., 3rd. (2001) Nmr probes of molecular dynamics: overview and comparison with other techniques, *Annu. Rev. Biophys. Biomol. Struct. 30*, 129−155.
15. Palmer, A. G., 3rd (1997) Probing molecular motion by NMR, *Curr. Opin. Struct. Biol. 7*, 732−737.
16. Kay, L. E. (1998) Protein dynamics from NMR, *Nat. Struct. Biol. 5 Suppl.*, 513−517.
17. Altman, S., and Kirsebom, L. (1999) Ribonuclease P, in *The RNA World* (Gesteland, R. F., Cech, T. R., and Atkins, J. F., Eds.) pp 351−380, CSH Press, Cold Spring Harbor.
18. Frank, D. N., and Pace, N. R. (1998) Ribonuclease P: unity and diversity in a tRNA processing ribozyme, *Annu. Rev. Biochem. 67*, 153−180.
19. Kole, R., Baer, M. F., Stark, B. C., and Altman, S. (1980) E. coli RNAase P has a required RNA component, *Cell 19*, 881−887.
20. Talbot, S. J., and Altman, S. (1994) Gel retardation analysis of the interaction between C5 protein and M1 RNA in the formation of the ribonuclease P holoenzyme from Escherichia coli, *Biochemistry 33*, 1399−1405.
21. Westhof, E., Wesolowski, D., and Altman, S. (1996) Mapping in three dimensions of regions in a catalytic RNA protected from attack by an Fe(II)-EDTA reagent, *J. Mol. Biol. 258*, 600−613.
22. Tanaka, T., Ando, T., Haga, S., and Kikuchi, Y. (2004) Examining the bases of the J3/4 domain of Escherichia coli ribonuclease P, *Biosci. Biotechnol. Biochem. 68*, 1388−1392.
23. Peck-Miller, K. A., and Altman, S. (1991) Kinetics of the processing of the precursor to 4.5 S RNA, a naturally occurring substrate for RNase P from Escherichia coli, *J. Mol. Biol. 221*, 1−5.
24. Kurz, J. C., and Fierke, C. A. (2002) The affinity of magnesium binding sites in the Bacillus subtilis RNase P x pre-tRNA complex is enhanced by the protein subunit, *Biochemistry 41*, 9545−9558.
25. Kurz, J. C., Niranjanakumari, S., and Fierke, C. A. (1998) Protein component of Bacillus subtilis RNase P specifically enhances the affinity for precursor-tRNAAsp, *Biochemistry 37*, 2393−2400.
26. Crary, S. M., Niranjanakumari, S., and Fierke, C. A. (1998) The protein component of Bacillus subtilis ribonuclease P increases catalytic efficiency by enhancing interactions with the 5′ leader sequence of pre-tRNAAsp, *Biochemistry 37*, 9409−9416.
27. Niranjanakumari, S., Stams, T., Crary, S. M., Christianson, D. W., and Fierke, C. A. (1998) Protein component of the ribozyme ribonuclease P alters substrate recognition by directly contacting precursor tRNA, *Proc. Natl. Acad. Sci. U.S.A. 95*, 15212−15217.
28. Andrec, M., Montelione, G. T., and Levy, R. M. (2000) Lipari-Szabo mapping: A graphical approach to Lipari-Szabo analysis of NMR relaxation data using reduced spectral density mapping, *J. Biomol. NMR 18*, 83−100.
29. Henkels, C. H., Kurz, J. C., Fierke, C. A., and Oas, T. G. (2001) Linked folding and anion binding of the Bacillus subtilis ribonuclease P protein, *Biochemistry 40*, 2777−2789.
30. Farrow, N. A., Muhandiram, R., Singer, A. U., Pascal, S. M., Kay, C. M., Gish, G., Shoelson, S. E., Pawson, T., Forman-Kay, J. D., and Kay, L. E. (1994) Backbone dynamics of a free and phosphopeptide-complexed Src homology 2 domain studied by 15N NMR relaxation, *Biochemistry 33*, 5984−6003.
31. Delaglio, F., Grzesiek, S., Vuister, G. W., Zhu, G., Pfeifer, J., and Bax, A. (1995) NMRPipe: a multidimensional spectral processing system based on UNIX pipes, *J. Biomol. NMR 6*, 277−293.
32. Johnson, B. A. (2004) Using NMRView to visualize and analyze the NMR spectra of macromolecules, *Methods Mol. Biol. 278*, 313−352.
33. Cavanagh, J., Fairbrother, W. J., Palmer, A. G., and Skelton, N. J. (1996) *Protein NMR Spectroscopy: Principles and Practice*, Academic Press, Inc., San Diego.
34. Abragam, A. (1961) *Principles of Nuclear Magnetism*, Clarendon Press, Oxford.
35. Hiyama, Y., Niu, C.-H., Silverton, J. V., Bavoso, A., and Torchia, D. A. (1988) Determination of ^{15}N chemical shift tensor via ^{15}N-^{2}H dipolar coupling in Boc-glycylglycyl[^{15}N]glycine benzyl ester, *J. Am. Chem. Soc. 110*, 2378−2383.
36. Farrow, N. A., Zhang, O., Szabo, A., Torchia, D. A., and Kay, L. E. (1995) Spectral density function mapping using 15N relaxation data exclusively, *J. Biomol. NMR 6*, 153−162.
37. Peng, J. W., and Wagner, G. (1992) Mapping of the spectral densities of N-H bond motions in eglin c using heteronuclear relaxation experiments, *Biochemistry 31*, 8571−8586.
38. Farrow, N. A., Zhang, O., Forman-Kay, J. D., and Kay, L. E. (1995) Comparison of the backbone dynamics of a folded and an unfolded SH3 domain existing in equilibrium in aqueous buffer, *Biochemistry 34*, 868−878.
39. Ishima, R., and Nagayama, K. (1995) Protein backbone dynamics revealed by quasi spectral density function analysis of amide N-15 nuclei, *Biochemistry 34*, 3162−3171.
40. Bevington, P. R. (1969) *Data Reduction and Error Analysis for the Physical Sciences*, McGraw-Hill Book Company, New York.
41. Zhang, P., Dayie, K. T., and Wagner, G. (1997) Unusual lack of internal mobility and fast overall tumbling in oxidized flavodoxin from Anacystis nidulans, *J. Mol. Biol. 272*, 443−455.
42. Amezcua, C. A., Harper, S. M., Rutter, J., and Gardner, K. H. (2002) Structure and interactions of PAS kinase N-terminal PAS domain: model for intramolecular kinase regulation, *Structure (Cambridge) 10*, 1349−1361.
43. Lipari, G., and Szabo, A. (1982) Model-Free Approach to the Interpretation of Nuclear Magnetic Resonance Relaxation in Macromolecules. 1. Theory and Range of Validity, *J. Am. Chem. Soc. 104*, 4546−4559.
44. Lipari, G., and Szabo, A. (1982) Model-Free Approach to the Interpretation of Nuclear Magnetic Resonance Relaxation in Macromolecules. 2. Analysis of Experimental Results, *J. Am. Chem. Soc. 104*, 4559−4570.
45. Mandel, A. M., Akke, M., and Palmer, A. G., 3rd. (1995) Backbone dynamics of Escherichia coli ribonuclease HI: correlations with structure and function in an active enzyme, *J. Mol. Biol. 246*, 144−163.
46. Clore, G. M., Szabo, A., Bax, A., Kay, L. E., Driscoll, P. C., and Gronenborn, A. M. (1990) Deviations from the Simple Two-Parameter Model-Free Approach to the Interpretation of Nitrogen-15 Nuclear Magnetic Relaxation of Proteins, *J. Am. Chem. Soc. 112*, 4989−4991.
47. Hanson, W. M., Beeser, S. A., Oas, T. G., and Goldenberg, D. P. (2003) Identification of a residue critical for maintaining the functional conformation of BPTI, *J. Mol. Biol. 333*, 425−441.
48. Schurr, J. M., Babcock, H. P., and Fujimoto, B. S. (1994) A test of the model-free formulas. Effects of anisotropic rotational diffusion and dimerization, *J. Magn. Reson. B 105*, 211−224.
49. Kay, L. E., Torchia, D. A., and Bax, A. (1989) Backbone dynamics of proteins as studied by 15N inverse detected heteronuclear NMR spectroscopy: application to staphylococcal nuclease, *Biochemistry 28*, 8972−8979.
50. Fushman, D., Ohlenschlager, O., and Ruterjans, H. (1994) Determination of the backbone mobility of ribonuclease T1 and its 2′GMP complex using molecular dynamics simulations and NMR relaxation data, *J. Biomol. Struct. Dyn. 11*, 1377−1402.
51. Tjandra, N., Feller, S. E., Pastor, R. W., and Bax, A. (1995) Rotational Diffusion Anisotropy of Human Ubiquitin from ^{15}N NMR Relaxation, *J. Am. Chem. Soc. 117*, 12562−12566.
52. Bruschweiler, R., Liao, X., and Wright, P. E. (1995) Long-range motional restrictions in a multidomain zinc-finger protein from anisotropic tumbling, *Science 268*, 886−889.
53. Stams, T., Niranjanakumari, S., Fierke, C. A., and Christianson, D. W. (1998) Ribonuclease P protein structure: evolutionary origins in the translational apparatus, *Science 280*, 752−755.
54. Ye, J., Mayer, K. L., and Stone, M. J. (1999) Backbone dynamics of the human CC-chemokine eotaxin, *J. Biomol. NMR 15*, 115−124.
55. Clore, G. M., Driscoll, P. C., Wingfield, P. T., and Gronenborn, A. M. (1990) Analysis of the backbone dynamics of interleukin-1 beta using two-dimensional inverse detected heteronuclear 15N-1H NMR spectroscopy, *Biochemistry 29*, 7387−7401.
56. Brown, J. W. (1998) The ribonuclease P database, *Nucleic Acids Res. 26*, 351−352.
57. Richardson, J. S. (1985) Describing patterns of protein tertiary structure, *Methods Enzymol. 115*, 341−358.

58. Mulder, F. A., Mittermaier, A., Hon, B., Dahlquist, F. W., and Kay, L. E. (2001) Studying excited states of proteins by NMR spectroscopy, *Nat. Struct. Biol. 8*, 932−935.
59. Wang, C., Grey, M. J., and Palmer, A. G., 3rd. (2001) CPMG sequences with enhanced sensitivity to chemical exchange, *J. Biomol. NMR 21*, 361−366.
60. Loria, J. P., Rance, M., and Palmer, A. G., 3rd. (1999) A Relaxation-Compensated Carr-Purcell-Meiboom-Gill Sequence for Characterizing Chemical Exchange by NMR Spectroscopy, *J. Am. Chem. Soc. 121*, 2331−2332.
61. Akke, M. (2002) NMR methods for characterizing microsecond to millisecond dynamics in recognition and catalysis, *Curr. Opin. Struct. Biol. 12*, 642−647.
62. Botuyan, M. V., Mer, G., Yi, G. S., Koth, C. M., Case, D. A., Edwards, A. M., Chazin, W. J., and Arrowsmith, C. H. (2001) Solution structure and dynamics of yeast elongin C in complex with a von Hippel-Lindau peptide, *J. Mol. Biol. 312*, 177−186.
63. Kristensen, S. M., Siegal, G., Sankar, A., and Driscoll, P. C. (2000) Backbone dynamics of the C-terminal SH2 domain of the p85alpha subunit of phosphoinositide 3-kinase: effect of phosphotyrosine-peptide binding and characterization of slow conformational exchange processes, *J. Mol. Biol. 299*, 771−788.
64. Katahira, M., Miyanoiri, Y., Enokizono, Y., Matsuda, G., Nagata, T., Ishikawa, F., and Uesugi, S. (2001) Structure of the C-terminal RNA-binding domain of hnRNP D0 (AUF1), its interactions with RNA and DNA, and change in backbone dynamics upon complex formation with DNA, *J. Mol. Biol. 311*, 973−988.
65. Zhu, L., Hu, J., Lin, D., Whitson, R., Itakura, K., and Chen, Y. (2001) Dynamics of the Mrf-2 DNA-binding domain free and in complex with DNA, *Biochemistry 40*, 9142−9150.
66. Eisenmesser, E. Z., Bosco, D. A., Akke, M., and Kern, D. (2002) Enzyme dynamics during catalysis, *Science 295*, 1520−1523.
67. Rozovsky, S., Jogl, G., Tong, L., and McDermott, A. E. (2001) Solution-state NMR investigations of triosephosphate isomerase active site loop motion: ligand release in relation to active site loop dynamics, *J. Mol. Biol. 310*, 271−280.
68. Lu, J., Lin, C. L., Tang, C., Ponder, J. W., Kao, J. L., Cistola, D. P., and Li, E. (2000) Binding of retinol induces changes in rat cellular retinol-binding protein II conformation and backbone dynamics, *J. Mol. Biol. 300*, 619−632.
69. Feher, V. A., and Cavanagh, J. (1999) Millisecond-timescale motions contribute to the function of the bacterial response regulator protein Spo0F, *Nature 400*, 289−293.
70. van Tilborg, P. J., Mulder, F. A., de Backer, M. M., Nair, M., van Heerde, E. C., Folkers, G., van der Saag, P. T., Karimi-Nejad, Y., Boelens, R., and Kaptein, R. (1999) Millisecond to microsecond time scale dynamics of the retinoid X and retinoic acid receptor DNA-binding domains and dimeric complex formation, *Biochemistry 38*, 1951−1956.
71. Nagata, T., Kanno, R., Kurihara, Y., Uesugi, S., Imai, T., Sakakibara, S., Okano, H., and Katahira, M. (1999) Structure, backbone dynamics and interactions with RNA of the C-terminal RNA-binding domain of a mouse neural RNA-binding protein, Musashi1, *J. Mol. Biol. 287*, 315−330.
72. Lu, J., and Hall, K. B. (1997) Tertiary structure of RBD2 and backbone dynamics of RBD1 and RBD2 of the human U1A protein determined by NMR spectroscopy, *Biochemistry 36*, 10393−10405.
73. Kazantsev, A. V., Krivenko, A. A., Harrington, D. J., Holbrook, S. R., Adams, P. D., and Pace, N. R. (2005) Crystal structure of a bacterial ribonuclease P RNA, *Proc. Natl. Acad. Sci. U.S.A. 102*, 13392−13397.
74. Torres-Larios, A., Swinger, K. K., Krasilnikov, A. S., Pan, T., and Mondragon, A. (2005) Crystal structure of the RNA component of bacterial ribonuclease P, *Nature 437*, 584−587.
75. Baer, M. F., Wesolowski, D., and Altman, S. (1989) Characterization in vitro of the defect in a temperature-sensitive mutant of the protein subunit of RNase P from Escherichia coli, *J. Bacteriol. 171*, 6862−6866.
76. Gopalan, V., Baxevanis, A. D., Landsman, D., and Altman, S. (1997) Analysis of the functional role of conserved residues in the protein subunit of ribonuclease P from Escherichia coli, *J. Mol. Biol. 267*, 818−829.
77. Gopalan, V., Golbik, R., Schreiber, G., Fersht, A. R., and Altman, S. (1997) Fluorescence properties of a tryptophan residue in an aromatic core of the protein subunit of ribonuclease P from Escherichia coli, *J. Mol. Biol. 267*, 765−769.
78. Gopalan, V., Kuhne, H., Biswas, R., Li, H., Brudvig, G. W., and Altman, S. (1999) Mapping RNA-protein interactions in ribonuclease P from Escherichia coli using electron paramagnetic resonance spectroscopy, *Biochemistry 38*, 1705−1714.
79. Tsai, H. Y., Masquida, B., Biswas, R., Westhof, E., and Gopalan, V. (2003) Molecular modeling of the three-dimensional structure of the bacterial RNase P holoenzyme, *J. Mol. Biol. 325*, 661−675.
80. Biswas, R., Ledman, D. W., Fox, R. O., Altman, S., and Gopalan, V. (2000) Mapping RNA-protein interactions in ribonuclease P from Escherichia coli using disulfide-linked EDTA-Fe, *J. Mol. Biol. 296*, 19−31.
81. Niranjanakumari, S., Day-Storms, J. J., Ahmed, M., Hsieh, J., Zahler, N. H., Venters, R. A., and Fierke, C. A. (2007) Probing the architecture of the B. subtilis RNase P holoenzyme active site by cross-linking and affinity cleavage, *RNA 13*, 521−535.
82. Spolar, R. S., and Record, M. T., Jr. (1994) Coupling of local folding to site-specific binding of proteins to DNA [see comments], *Science 263*, 777−784.
83. Sun, L., Campbell, F. E., Zahler, N. H., and Harris, M. E. (2006) Evidence that substrate-specific effects of C5 protein lead to uniformity in binding and catalysis by RNase P, *EMBO J. 25*, 3998−4007.
84. Getz, M. M., Andrews, A. J., Fierke, C. A., and Al-Hashimi, H. M. (2007) Structural plasticity and Mg2+ binding properties of RNase P P4 from combined analysis of NMR residual dipolar couplings and motionally decoupled spin relaxation, RNA *13*, 251−266.
85. Millet, O., Loria, J. P., Kroenke, C. D., Pons, M., and Palmer, A. G., 3rd. (2000) The static magnetic field dependence of chemical exchange linebroadening defines the NMR chemical shift time scale, *J. Am. Chem. Soc. 122*, 2867−2877.

BI701425N